



Cite this: DOI: 10.1039/d2tc02627a

# Transparent fluoride glass-ceramics with phase-selective crystallization for middle IR photonics†

Longfei Zhang,<sup>‡ab</sup> Yang Sun,<sup>‡cd</sup> Yiguang Jiang,<sup>\*a</sup> Bo Da,<sup>e</sup> Juan Du,<sup>af</sup> Shuaipeng Wang,<sup>a</sup> Sisheng Qi,<sup>a</sup> Zhiyong Yang,<sup>a</sup> Long Zhang<sup>id</sup><sup>\*af</sup> and Jin He<sup>\*af</sup>

Crystallization in glass is a fundamental topic in materials science, yielding the beauty and richness of crystals in glass for broad applications. However, controlling the crystallization in fluoride glasses remains a challenge owing to their low glass-forming ability. We fabricate transparent fluorindate glass-ceramics (FGCs) with phase-selective crystallization ( $\text{SrF}_2$ ,  $\text{CaF}_2$  and  $\text{MgF}_2$ ) by a general one-step strategy. The alkaline-earth cations with high field strength are utilized to engineer the phase separation which induce subsequent phase-selective crystallization. The *ab initio* molecular dynamics revealed the heterogeneous distribution of Sr/Y–F regions and diverse diffusion rates of different elements in fluoride glass melt, providing fundamental insights into phase-separation at the atomic scale. Rapid quenching is employed to regulate the crystal growth in spontaneous crystallization during the cooling stage. The crystal morphology, element distribution, lattice parameters and simulated atomic structure in FGCs further elucidate the phase-separation mechanism, thermodynamics and kinetics in rapid quenching. The new FGCs manifest enhanced mechanical and chemical stability and do not sacrifice the excellent optical performance compared to the parent fluorindate glass. Numerous optical applications with superior properties in MIR photonics have been demonstrated. This sets the stage for phase-separation chemistry to yield a diverse selection of desired crystals precipitated from fluoride glass.

Received 22nd June 2022,  
Accepted 17th August 2022

DOI: 10.1039/d2tc02627a

rsc.li/materials-c

## 1. Introduction

Controlled crystallization of glasses is a basic area within glass science. Essentially glass ceramics (GCs) represent optimal properties because they possess zero porosity, high strength, excellent chemical durability and tunable luminescence.<sup>1–4</sup> As the only transparent material in the continuum spectrum from ultraviolet up to middle IR (MIR) region, fluoride glasses offer an appealing alternative to prototypical silica glasses for a set of

photonic applications.<sup>5,6</sup> However, fluoride glasses suffer from low glass-forming ability, weak mechanical properties and poor chemical resistance, which obstruct their widespread application in photonics.<sup>7</sup> It has been a great challenge to fabricate transparent fluoride glass ceramics (FGCs). In the classical melting–quenching–annealing two-step procedure, the poor thermal stability of fluoride glass results in the uncontrollable crystallization during the annealing. Random nucleation or spinodal decomposition would occur near the glass transition temperature ( $T_g$ ), resulting in the serious deterioration of transparency.<sup>8–11</sup> To date, the successful controllable crystallization of fluoride crystals are mostly limited to oxy-fluoride systems – fluoride crystals in oxide glass.<sup>12–15</sup> Very few attempts at transparent fluorozirconate GCs have been reported via careful tailoring of composition and annealing process.<sup>8,9,16–20</sup> However, these advancements were restricted by narrow composition range, uncontrollable crystal phase, and lack of an atomic-level understanding in crystallization towards rational materials design. Therefore, a general approach for producing transparent FGCs where there is flexibility to control the crystallization phase has been long-awaited.

Enabling the precisely controlled crystallization and the development of new FGCs were governed by an appropriate

<sup>a</sup> Key Laboratory of Materials for High Power Lasers and State Key Laboratory of High Field Laser Physics, Shanghai Institute of Optics and Fine Mechanics, Chinese Academy of Sciences, Shanghai 201800, China.

E-mail: jiangyiguang@siom.ac.cn, lzhang@siom.ac.cn, jhe@siom.ac.cn

<sup>b</sup> Center of Materials Science and Optoelectronics Engineering, University of Chinese Academy of Sciences, Beijing 100049, China

<sup>c</sup> Department of Applied Physics and Applied Mathematics, Columbia University, New York, NY 10027, USA

<sup>d</sup> Department of Physics, Iowa State University, Ames, IA 50011, USA

<sup>e</sup> Research and Services Division of Materials Data and Integrated System, National Institute for Materials Science, 1-1 Namiki, Tsukuba, Ibaraki 305-0044, Japan

<sup>f</sup> Hangzhou Institute for Advanced Study, UCAS, Hangzhou, Zhejiang 310024, China

† Electronic supplementary information (ESI) available. See DOI: <https://doi.org/10.1039/d2tc02627a>

‡ Longfei Zhang and Yang Sun contributed equally to this work.

compositional design and optimal fabrication process. The two known fabrication strategies of GCs include the classical melting–quenching–annealing process and concurrent sintering–crystallization of glass particle compacts.<sup>9,21</sup> Recently, we developed a new facile one-step route with concurrent rapid-quenching–crystallization for the phase-selective crystallization in fluoride glass, which was achieved *via* the unique combination of liquid phase-separation engineering and rapid quenching.<sup>22–24</sup> Phase-separation, a pre-nucleating process without crystal formation, is used to trigger spontaneous crystallization in a fluoride glass melt during the cooling stage.<sup>25,26</sup> This is achieved *via* the introduction of specific cations with selection of field strength that can induce the desired phase separation.<sup>27,28</sup> As the heavy elements result in the low viscosity of the fluoride glass melt and make them vulnerable to random spontaneous crystallization during the cooling stage, a rapid quenching was employed to accelerate the cooling rate which would regulate the crystal growth. With this tailored spontaneous crystallization by rapid quenching route, we successfully achieved the phase-selective crystallization in several typical fluoride glasses (fluoroindate, fluorozirconate *etc.*), manifesting the impressive potential to be a general technique for the fabrication of FGCs. Compared with parent fluoride glasses, these new FGCs exhibit exceptional optical properties, enhanced mechanical and thermal properties, due to the selective precipitation of the desired crystals.<sup>22,23</sup> All this calls for further study aimed at creating a library of new FGCs and unveiling the thermodynamics and kinetics mechanism of the new fabrication strategy on the atomic scale.

Compared with the classic fluorozirconate glass, the ultra-wide MIR transmission window and lower maximum phonon energy of fluoroindate glass make it an ideal candidate for a new generation of fiber lasers and laser power delivery media.<sup>29</sup> Alkaline-earth fluoride crystals were selected as the target crystals as they were considered the star photonic materials owing to the unique combination of low phonon energy, high rare-earth solubility and relatively weak crystal field.<sup>30,31</sup> Notably, alkaline-earth metal cations have a high field strength, which promotes the phase separation in the glass melt.<sup>27</sup> Here, we demonstrate the phase-selective crystallization of a set of alkaline-earth crystals including  $\text{SrF}_2$ ,  $\text{CaF}_2$ , and  $\text{MgF}_2$  in fluoroindate glass *via* the one-step concurrent rapid-quenching–crystallization route. *Ab initio* molecular dynamics (AIMD) simulations on the parent liquid state of fluoride glass further predicted the phase-separation at the atomic scale. The variation of the crystal morphologies in FGCs indicates that the crystal growth during the melt-quenching was driven by the thermodynamic parameters at the solid–liquid interface. Element distribution and simulated atomic structure were identified, all unveiling the phase separation chemistry, thermodynamics and kinetics in the fabrication process. Such FGCs manifest an enhancement in both mechanical property and chemical stability without sacrificing the high transmittance. This study deepens our fundamental insight into the phase separation–crystallization relationship in glass science, which offers a novel route towards engineering GCs with the desired crystals.

## 2. Experimental section

### 2.1 FGC Fabrication

The compositions of FGCs were  $25\text{InF}_3\text{-}20\text{BaF}_2\text{-}20\text{SrF}_2\text{-}30\text{ZnF}_2\text{-}5\text{YF}_3$  (FGCSrF<sub>2</sub>),  $25\text{InF}_3\text{-}20\text{BaF}_2\text{-}10\text{SrF}_2\text{-}30\text{ZnF}_2\text{-}5\text{YF}_3\text{-}10\text{CaF}_2$  (FGCCaF<sub>2</sub>), and  $25\text{InF}_3\text{-}20\text{BaF}_2\text{-}15\text{SrF}_2\text{-}30\text{ZnF}_2\text{-}5\text{YF}_3\text{-}5\text{MgF}_2$  (FGCMgF<sub>2</sub>). The composition of fluoroindate glass composition was  $25\text{InF}_3\text{-}35\text{BaF}_2\text{-}15\text{SrF}_2\text{-}20\text{ZnF}_2\text{-}5\text{YF}_3$  (FGInF<sub>3</sub>), which was used for performance comparison. Batches of 20 g were melted in a Pt–Au crucible at the temperature of  $\sim 1150$  K for 25 min. The FGC samples were obtained by rapid quenching, which involved pouring the glass melt between the two aluminum molds. While the comparative samples were obtained by traditional quenching, which consisted in directly pouring the glass melt onto the aluminum mold. After that, the samples were annealed at  $\sim 535$  K for 4 h to remove the stress. Then they were polished to 1 mm thickness for measurements.

### 2.2 Theoretical simulations

AIMD simulations were performed to simulate the liquid states of FGCs with chemical composition  $25\text{InF}_3\text{-}20\text{BaF}_2\text{-}20\text{SrF}_2\text{-}30\text{ZnF}_2\text{-}5\text{YF}_3$  (FGCSrF<sub>2</sub>). The density functional theory calculations in AIMD are performed using the Vienna *ab initio* simulation package (VASP).<sup>32</sup> The projected augmented-wave (PAW) method is used to describe the electron–ion interaction, and the generalized gradient approximation (GGA) in the Perdew–Burke–Ernzerhof (PBE) form is employed for the exchange–correlation energy functional. The  $\Gamma$  point was used to sample the Brillouin zone of the simulation cell containing 330 atoms. The constant number of atoms, volume and temperature (*NVT*) ensemble is applied with Nose–Hoover thermostats. The Verlet algorithm is used to integrate Newton's equation of motion, using a time step of 3 fs. The initial configuration is randomly generated and equilibrated for over 6000 time steps at 1750 K, which is much higher than the melting points. Then the sample is cooled down to 1150 K. The atomic structures at 1750 K, 1550 K, 1350 K and 1150 K are collected separately to perform further isothermal annealing for more than 12 000 time steps. The first 2000 time steps are not used in the analysis.

### 2.3 Materials characterization

The thermal behavior was testified by the thermogravimetric analyzer (EXSTAR SII: TG/DTA7300) at a heating rate of  $5\text{ K min}^{-1}$ ,  $10\text{ K min}^{-1}$ , and  $15\text{ K min}^{-1}$ . The phase composition characterization of the materials was performed by X-ray diffractometer (PANalytical X'Pert Pro Empyrean) with Cu–K $\alpha$  irradiation. The microscopic morphology observation and element characterization of the sample were performed by the field emission scanning electron microscopy equipped with EDS (FESEM, Hitachi S-4800). The in-line transmittance spectra were obtained by Fourier-transform spectroscopy (Nicolet). The up-conversion (UC) spectra and the mid-fluorescence emission of around  $2.9\text{ }\mu\text{m}$  were measured using the instrument FLSP 920 (Edinburgh Instruments Ltd).

### 3. Results and discussion

#### 3.1 Design principles for selective phase-separation engineering

The immiscible, early phase-separated domains are formed through the competition between different metal cations when bonding fluoride anions in the multi-component fluoride melt.<sup>27</sup> The formation of phase-separated domains would facilitate heterogeneous nucleation *via* decreasing the activation energy.<sup>28</sup> Therefore, the phase-selective crystallization in the fabrication of FGCs is achieved by introducing specific metal cations with high strength field to induce specific phase separation. Here, we briefly describe the composition design principles in engineering the phase separation in the fluoride glass melt. The alkali earth cations were selected to engineer phase separation based on the following considerations: alkaline-earth metal cations in the fluorindate glass system have a high field strength  $Z$  that can easily capture F<sup>-</sup> and form new phase-separated domains. As illustrated in Fig. 1a, the green area represents the phase-separated alkaline-earth fluoride region. The field strength  $Z$  of the alkaline-earth metal group Mg, Ca, Sr and Ba are 2.56, 1.89, 1.57 and 1.40, respectively. It was reported when  $Z$  is greater than 1.4 (e.g. Mg<sup>2+</sup>, Ca<sup>2+</sup>, and Sr<sup>2+</sup>), a stable immiscible region would be formed above liquidus temperature.<sup>27</sup> As the  $Z$  of Ba<sup>2+</sup> (1.40) is located at the boundary, the introduction of Ba<sup>2+</sup> cations would probably lead to a metastable immiscible region. Therefore, based on the field strength dependent phase separation mechanism, we choose MgF<sub>2</sub>, CaF<sub>2</sub> and SrF<sub>2</sub> as the target crystal phases, and the system containing BaF<sub>2</sub> was used as a control experiment.

The atomic mechanism of phase separation in the fluoride glass melt is necessary for the rational design of the FGCs. From the metallic glasses and glass-forming models, it has been shown that the mechanism of phase separation and crystallization during the rapid quenching can originate from the structural and chemical ordering prevailing in the early liquid state.<sup>33–35</sup> However, the atomic structure of amorphous fluoride is rarely simulated due to its complex chemical composition and the limitation of fluoride force fields. Here, the

AIMD simulations of FGCSrF<sub>2</sub> melts are performed to reveal the phase separation mechanism in the liquid state. The atomic structure of FGCSrF<sub>2</sub> at 1150 K, which locates in the experimental preparation temperature range (1123 K to 1173 K), is shown in Fig. 1b. Fluoride clusters centered by different metal cations show a clear heterogeneous spatial distribution in the liquid structure. A separation between Sr/Y-rich regions and Sr/Y-poor regions (highlighted by the contour plot in Fig. 1b and isosurface in Fig. S1a, ESI†) were observed. Therefore, the first-principles simulation, regardless of time and length-scale limitations, has already indicated the presence of phase separation in the FGCSrF<sub>2</sub> melt. We further calculated the atomic diffusion coefficient from the simulation, as shown in Fig. S1b (ESI†). In and Zn showed a higher mean square displacement than Sr and Y. The slower dynamics of Sr/Y should maintain the Sr/Y rich region as a stable state during the quenching process. The accelerated diffusion rates of In and Zn can further promote the formation of Sr–Y rich phases in crystallization. The AIMD simulations indicate that the phase separation process originates from the chemical heterogeneity in the FGCSrF<sub>2</sub> melt, in which Y cations participate in the crystallization of SrF<sub>2</sub>.

#### 3.2 Concurrent rapid-quenching-crystallization process

The phase-selective crystallization from the parent glass melt is governed by a balance between the thermodynamic driving force and the energy penalty for creating new solid–liquid interfaces. As revealed in the above section, the phase separation in fluorindate glass melt was induced by the high field strength of alkaline-earth cations and different diffusion rates of atoms. After the phase separation domains formed in the melt, the atoms migrate to form the nucleus and subsequent spontaneous crystallization occurs under appropriate under-cooling and supersaturation conditions.

To quantitatively evaluate the nucleation barrier, the crystallization activation energy ( $E_c$ ) of FGCs is calculated by JMA (Johnson–Mehl–Avrami) equation<sup>36</sup> based on the differential thermal analysis data, as shown in Fig. S2 (ESI†). The results, displayed in Table S1, (ESI†) show that the order of  $E_c$  is

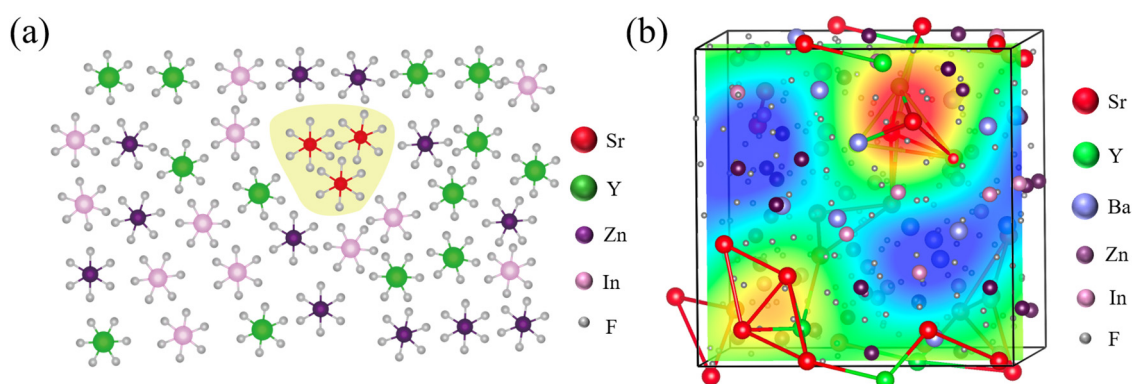


**Fig. 1** Design principles of phase separation at the atomic scale. (a) Design principles of phase separation for FGCs; (b) atomic configuration from AIMD simulation of FGCSrF<sub>2</sub> at  $T = 1150$  K. The Sr and Y pairs are connected. The contour indicates the Sr/Y density at a 2D plane where red shows the Sr/Y-rich region and blue shows the Sr/Y-poor region.

FGCMgF<sub>2</sub> (310.3 KJ mol<sup>-1</sup>) < FGCCaF<sub>2</sub> (330 KJ mol<sup>-1</sup>) < FGCSrF<sub>2</sub> (332 KJ mol<sup>-1</sup>), which is consistent with the order of the cation field strength. The higher tendency of phase separation decreases the crystal activation energy. This result indicates the nucleus formation is closely correlated with the phase separation in glass melt. Moreover, the alkaline-earth cations act as glass modifiers, which tend to be randomly distributed in the glass matrix, thus effectively favouring their diffusion in the nucleation and crystal growth process.

Quenching is a rapid cooling process of high-temperature states to prevent the transformation of thermodynamical equilibrium phases. It can reduce the time window of undesired reactions, especially when the undesired phases are thermodynamically preferred. In the fluoride glass system, the low bonding strength of metal fluoride results in the low viscosity of the glass melt, which facilitates the atom diffusions towards a higher crystallization tendency.<sup>7</sup> Therefore, after phase separation occurred in the glass melt, a rapid quenching was required to tailor the spontaneous crystallization for the precipitation of desired crystals in the cooling stage. The rapid quenching was implemented by pouring the glass melt between two metal pieces preheated at ~535 K instead of the traditional melt-quenching method on a single piece mold, as shown in Fig. 2b. The two sides quenching notably increase the contact area for the glass melt, ensuring a high cooling rate and homogeneous cooling.<sup>37,38</sup> This high-speed frozen of glass network efficiently impedes the diffusion of atoms, thus avoiding the random overgrowth of crystals.

The fabricated FGCs maintain good transmittance from visible range (Fig. S3, ESI<sup>†</sup>) to the IR range (Fig. 2d). In particular, in the MIR range (3–8.5 μm), the transmittance reaches above 80%, which demonstrates the promising potential in the MIR applications. The XRD pattern (Fig. 2e) demonstrates that the target crystal phases of SrF<sub>2</sub>, CaF<sub>2</sub> and MgF<sub>2</sub> were successfully precipitated in related FGC samples, according to the PDF cards. The slight shifts of the diffraction peaks were observed in all SrF<sub>2</sub>, CaF<sub>2</sub> and MgF<sub>2</sub> crystals, respectively. This observation can be well explained by the AIMD simulations that Y cations participate in the formation of SrF<sub>2</sub> phase-separated regions. The entrance of impurity cations into the lattice of the alkaline-earth fluoride crystals is further proved in EDS mapping in the next section as well. As predicted, the FGCBaF<sub>2</sub> system exhibits the coexistence of two crystal phases-BaF<sub>2</sub> and Ba<sub>2</sub>ZnF<sub>6</sub>, as shown in Fig. S4 (ESI<sup>†</sup>). The control experiment further indicates the phase-selective crystallization is governed by our proposed field strength dependent phase-separation mechanism.

On the other hand, the crystallization of the parent fluorindate glass is uncontrollable in the classical melting-quenching-annealing route, as shown in Fig. 2a. After annealing of fluorindate glass (FGInF<sub>3</sub>-AN) around 340 °C for 4 hours, random crystal phases are precipitated, as presented in Fig. S5, (ESI<sup>†</sup>) which is a common phenomenon in the fluoride system owing to the atomic rearrangement at the crystallization temperature. Moreover, the spontaneous crystallization behavior of the FGC melt with the same designed composition (FGCSrF<sub>2</sub>-MQ, FGCCaF<sub>2</sub>-MQ and FGCMgF<sub>2</sub>-MQ) in one side melt-quenching is investigated and their XRD

patterns are shown in Fig. S6 (ESI<sup>†</sup>). They also show a random distribution of crystallization peaks, which indicates the low cooling rates provide enough time window for the atoms of the remaining phase to migrate to form complex crystal phases. It leads to the uncontrollable spontaneous crystallization of the remaining glass phase in the melt. Therefore, both compositional design and rapid quenching are crucial for the phase-selective crystallization of alkaline-earth fluoride crystals in fluorindate glass. Further considerations of this important far-from-equilibrium step and the resultant compositional dependent crystal morphologies are discussed later.

### 3.3 The structure of the FGCs

We next consider the FGC micro-structure and composition, which reveals the non-trivial underlying mechanism in the concurrent rapid-quenching-crystallization process and their optical properties. The SEM and EDS of the samples were used to characterize the crystal morphology and element distribution. The SEM picture presents the variation of the crystal size and morphology in FGCSrF<sub>2</sub>, FGCCaF<sub>2</sub> and FGCMgF<sub>2</sub>, as shown in Fig. 3. The crystal size increases with the order of SrF<sub>2</sub> (~1 μm), CaF<sub>2</sub> (~50 μm) and MgF<sub>2</sub> (~200 μm). Three diverse morphologies, SrF<sub>2</sub> crystals in sphere, CaF<sub>2</sub> crystals in petal-shape and MgF<sub>2</sub> crystals in needle-shape, were observed, respectively. This unique variation in morphology reflects that the crystallization dynamics are correlated with the composition in the rapid quenching process. According to the solidification theory, the crystal morphology is determined by the heat transfer of the latent heat at the solid-liquid interface of crystal growth. The latent heat of SrF<sub>2</sub>, CaF<sub>2</sub> and MgF<sub>2</sub> are 18 kJ mol<sup>-1</sup>, 29.7 kJ mol<sup>-1</sup> and 58.7 kJ mol<sup>-1</sup>, respectively.<sup>39</sup> For the SrF<sub>2</sub>, the isotropic spherical crystals are formed by evenly growth in all directions due to the relatively small heat release.<sup>40</sup> The larger latent heat leads to a higher temperature, lower viscosity and supersaturation concentration at the solid-liquid interface in the crystal growth. This nonequilibrium thermodynamic condition benefits the anisotropic dendritic growth.<sup>41</sup> Therefore, the dendritic petal-shape crystal grains of CaF<sub>2</sub> are formed with the increasing latent heat. As the latent heat of MgF<sub>2</sub> is almost double compared to CaF<sub>2</sub>, the higher temperature gradient accelerates the dendritic growth, and crystals tend to grow in the distance area.<sup>42,43</sup> This far-from-equilibrium thermodynamics at the crystal growth interface further facilitate the anisotropic crystal growth, which results in needle-shaped crystals with the size increased to 200 μm.

Further manifestations of phase-separation induced crystallization are observed in the element distribution of crystals in three FGCs. As we discussed above, the peak shifts were observed in the XRD patterns (Fig. 2e) of the precipitated crystal phase for SrF<sub>2</sub>, CaF<sub>2</sub> and MgF<sub>2</sub>. And AIMD simulation of the FGCSrF<sub>2</sub> melt reveals the entrance of Y cations into the SrF<sub>2</sub> crystal phase during phase separation. Here, the EDS mapping (Fig. 3a) provides the direct evidence to confirm that the impurity cations in SrF<sub>2</sub> crystal are mainly Y cations. Other metal cations are mainly distributed in the glass phase. The lattice distortion in the XRD is owing to the formation of solid



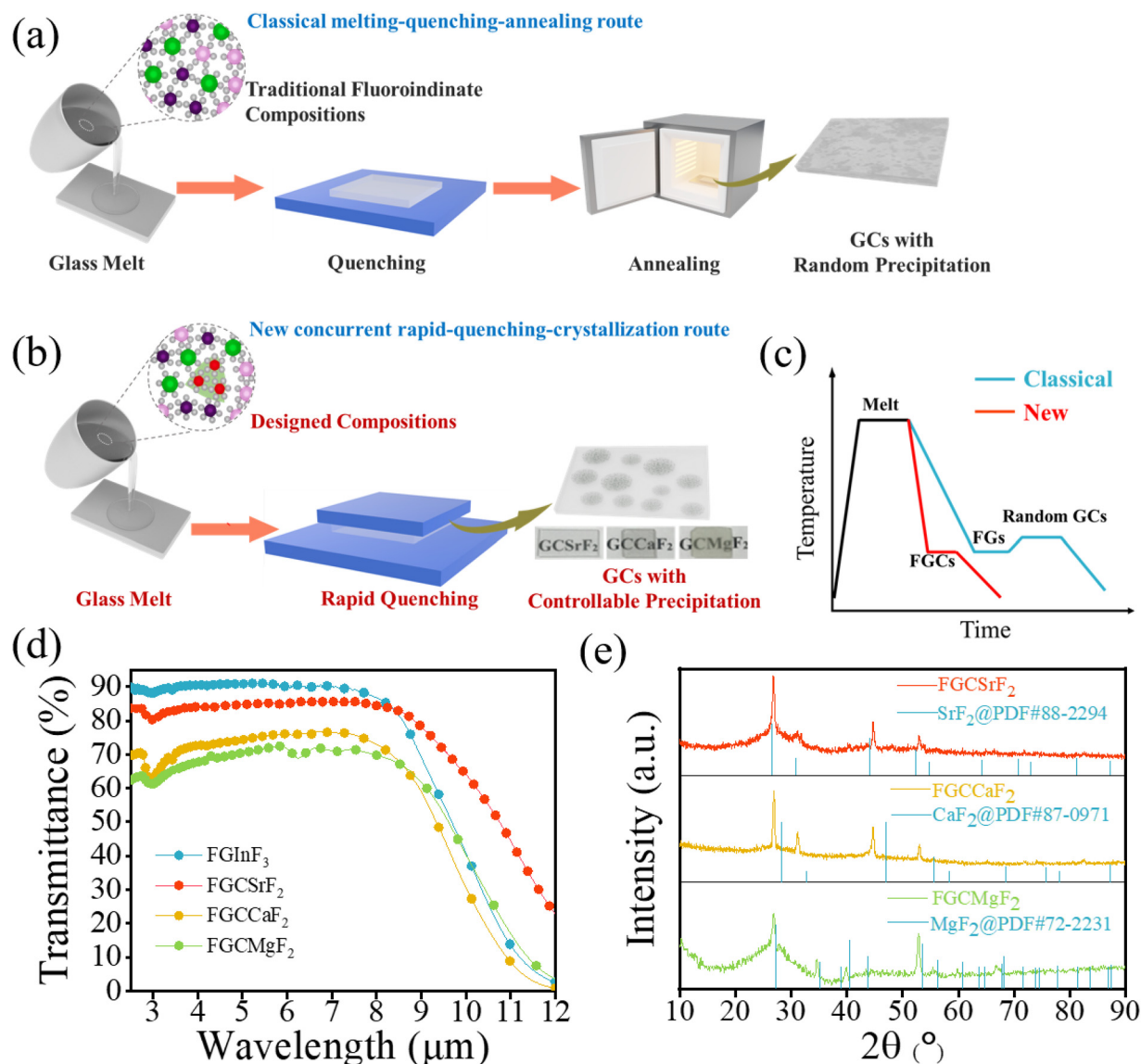


Fig. 2 The new concurrent rapid-quenching–crystallization route for fabricating transparent FGCs. (a) Fabrication of GCs with classical melting–quenching–annealing two step route; (b) fabrication of FGCs with the new concurrent rapid-quenching–crystallization route (inset: photo of the fabricated FGCs); (c) the GCs fabrication processes of classical and new route; (d) the in-line MIR transmittance of FGCs and fluorindate glass; (e) XRD patterns of the FGCs obtained by one-step route and the standard JCPDF cards: FGCSrF<sub>2</sub> and PDF#82-0640 of SrF<sub>2</sub> crystal, FGCCaF<sub>2</sub> and PDF#87-0971 of the CaF<sub>2</sub> crystal, and FGCMgF<sub>2</sub> and PDF#72-2231 of the MgF<sub>2</sub> crystal.

solution when Y<sup>3+</sup> enters into the SrF<sub>2</sub> lattice. This phenomenon agreed well with the AIMD simulation that the formation of Sr–Y-rich phase separated domains acted as the nucleus for the crystal growth. The impurity cations were also observed in FGCCaF<sub>2</sub> and FGCMgF<sub>2</sub>, providing further evidence that the similar crystallization mechanism induced by the formation of phase separation domains. The Sr and Y elements enrichment were observed in the CaF<sub>2</sub> crystals (Fig. 3b), and Zn enrichment was shown in MgF<sub>2</sub> crystals (Fig. 3c). The element distribution in three crystals well explains the peak shifts in all XRD patterns.

AIMD simulations provide detailed atomic structure of amorphous fluoride. Due to the time-scale difference between computer simulation and experiments, we simulate the liquid

state of FGC, which can be equilibrated much more easily compared to the glass state in the simulation. Pair correlation functions,  $g(r)$ , of FGCSrF<sub>2</sub> at 1150 K are calculated from the AIMD results. The pairs between the metal cations and F<sup>−</sup> anions are presented in Fig. 4. The first peaks of all the cations correspond to M–F (M = In, Ba, Sr, Zn, and Y), indicating that all the cations in the FGCSrF<sub>2</sub> are surrounded by F (see full  $g(r)$  in Fig. S7, ESI†). This is consistent with the previous study on fluoride glass,<sup>44,45</sup> which demonstrates that the *ab initio* simulation can be used as an effective method for studying the atomic structure of FGCs. Notably, as shown in Fig. 4a, In–F and Zn–F pairs show the smallest bond length of  $r = 1.90$  Å, which indicates that In and Zn have a similar coordination environment. The bond lengths of Y–F, Sr–F, and Ba–F are at

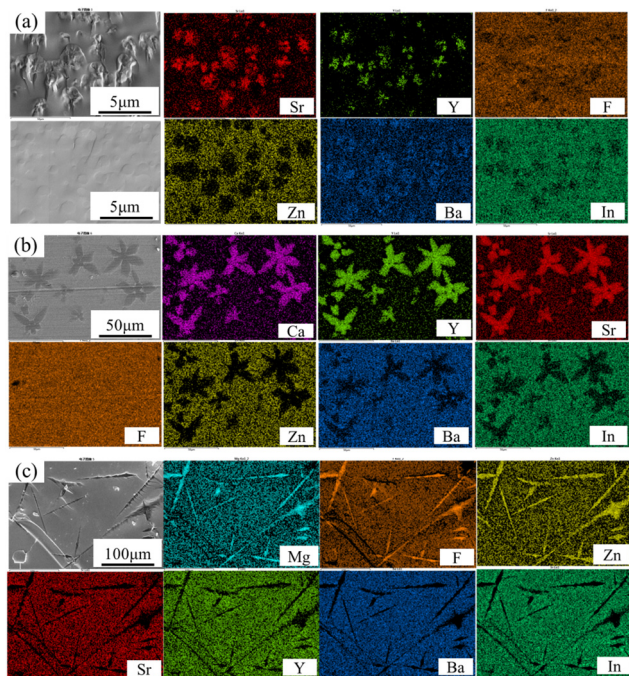


Fig. 3 Crystal morphology and elements distribution in FGCSrF<sub>2</sub>. (a) FGCSrF<sub>2</sub>. (b) FGCCaF<sub>2</sub>. (c) FGCMgF<sub>2</sub>. The scanning voltage is 10 kV. Picture in the lower left corner of (a) is the SEM image of the FGCSrF<sub>2</sub> sample.

$r = 2.15 \text{ \AA}$ ,  $r = 2.40 \text{ \AA}$ , and  $r = 2.59 \text{ \AA}$ , respectively. According to the first minima distance in  $g(r)$ , the distribution of F coordination numbers (CN) can be calculated, as presented in Fig. 4b. The CN of In and Zn are both  $\sim 6$ , respectively, so that both In and Zn maintain the octahedral structural units, the same as the fluoride glass.<sup>44</sup> This indicates that the network structure of FGCSrF<sub>2</sub> is identical to the fluoride glass matrix. It is worth noting that the CN of Sr increased to  $\sim 10$ , which is significantly higher than that in the fluoride glass (CN = 8). This variation can be attributed to the formation of the Sr–Y phase separation domains in which Sr captures the surrounding F from Y atoms, leading to the reduction of Y's CN (CN = 8).

We note the Y's CN in glass is 9 or 10.<sup>46</sup> In addition, XPS of FGInF<sub>3</sub> glass and FGCSrF<sub>2</sub> provides further information on the subtle structural changes. The F1s XPS spectra for the FGCSrF<sub>2</sub> and FGInF<sub>3</sub> glass are shown in Fig. S8 (ESI†). The peak of FGCSrF<sub>2</sub> shifts to the lower band energy, which indicates that more F atoms have bonded to the cation with the lower electron-attracting ability.<sup>47</sup> This is in line with the simulations that more F atoms are bonding to Sr than Y, which lowers the band energy as the electronegativity of Y<sup>3+</sup> is higher than Sr<sup>2+</sup>. The distribution of Sr and Y in the final atomic configuration at 1150 K is shown in Fig. 1b. To understand the Sr–Y network, the Sr and Y atomic distribution is coarse-grained to the atomic density  $D(\vec{r})$  by a Gaussian smearing scheme as<sup>48</sup>

$$D(\vec{r}) = \sum_i \left( \frac{1}{2\sigma^2\pi} \right)^{3/2} e^{-(\vec{r}-\vec{r}_i)^2/2\sigma^2} \quad (1)$$

where  $\vec{r}_i$  are the position of Sr and Y atoms.  $\sigma$  is set to  $3.4 \text{ \AA}$  so that the half-width at half maximum of the Gaussian function equals the position of the Sr–Y peak in the pair correlation function (see Fig. S7, ESI†). The spatial density shows a clear difference between Y/Sr-rich and Y/Sr-poor regions in Fig. 1b. The isosurface of the Sr–Y density also indicates that the Sr–Y network penetrates the sample and separates from the Y/Sr-poor regions (see Fig. S1a, ESI†).

### 3.4 FGCSrF<sub>2</sub> for MIR photonics

After establishing the successful fabrication and characterization of the FGCSrF<sub>2</sub>, we discuss their merits as MIR photonics materials. Owing to the uniform dispersion and low entropy of the crystal phase, GCs generally possess the enhanced mechanical properties and chemical resistance than the parent glass. As presented in Fig. 5a, the Vickers hardness values of FGCSrF<sub>2</sub>, FGCCaF<sub>2</sub>, FGCMgF<sub>2</sub>, and FGInF<sub>3</sub> are 272.8 HV, 313.9 HV, 289.8 HV and 261.5 HV, respectively. In addition, the chemical resistance of FGCSrF<sub>2</sub> was tested by the weight loss rate ( $\Delta W$ ) after keeping them in distilled water at  $98^\circ\text{C}$  for 10 h. The  $\Delta W$  of the FGCSrF<sub>2</sub>, FGCCaF<sub>2</sub>, FGCMgF<sub>2</sub>, and FGInF<sub>3</sub> are 0.06%, 0.21%, 0.73% and

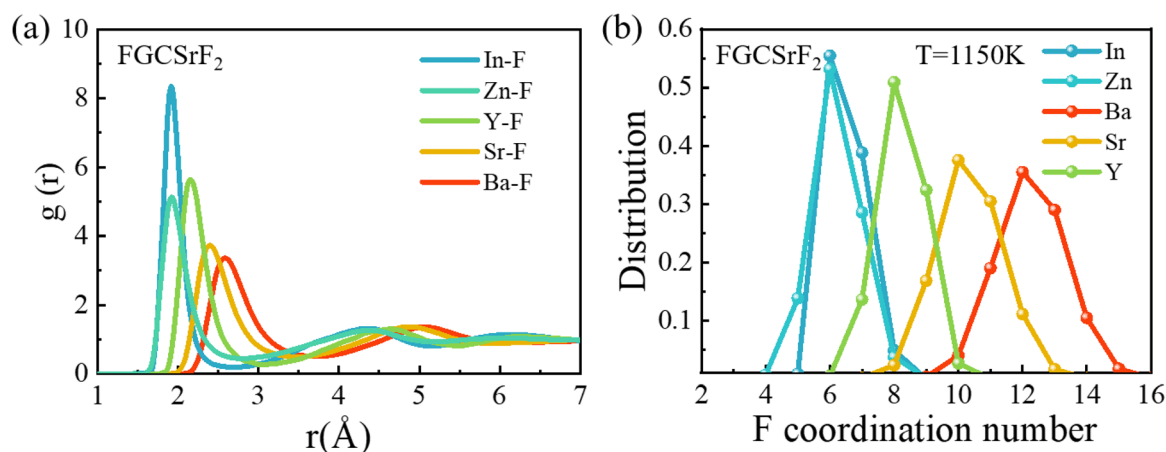


Fig. 4 Atomic structure of FGCSrF<sub>2</sub> via AIMD simulations. (a) Pair correlation function of atomic structure of FGCSrF<sub>2</sub>. (b) The CN of Cations in the FGCSrF<sub>2</sub>.

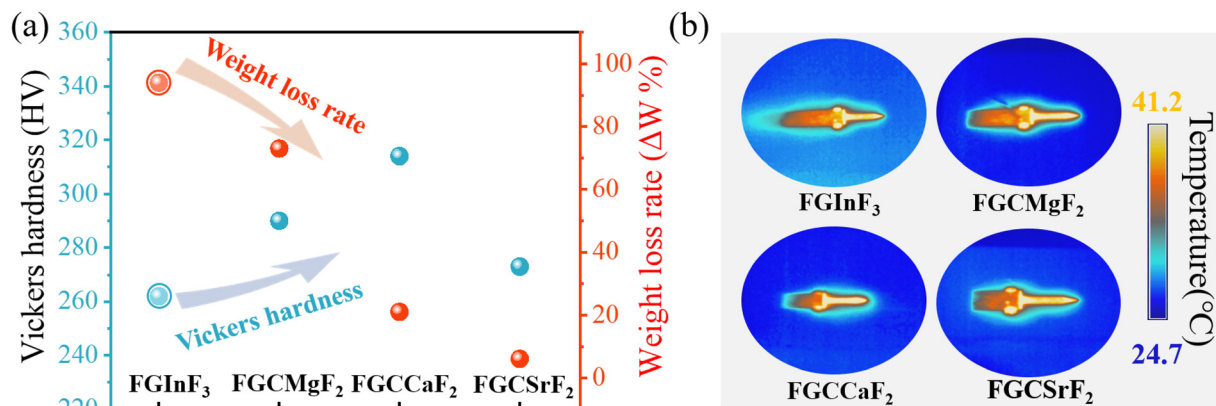


Fig. 5 Enhanced physicochemical properties and high optical quality of FGCs. (a) Corrosion resistance and Vickers hardness of FGCs and FGInF<sub>3</sub>. (b) Infrared thermography of FGCs and FGInF<sub>3</sub>.

0.94%, respectively. These data are further shown in Table S2 (ESI<sup>†</sup>). The expected enhanced mechanical and chemical properties of FGCs shows a significant advantage in extending the service environment.

Next, we consider the transparency, which in FGCs is influenced by structure and composition. Herein, we attributed the satisfactory transmittance of FGCs to the refractive index matching between fluoride crystal phase and fluoride glass matrix. The detailed refractive index data of the glass matrix and the crystal phase are listed in Table S3 (ESI<sup>†</sup>). Notably, the crystal and glass phases in FGCSrF<sub>2</sub> and FGCCaF<sub>2</sub> present a high consistency in refractive index. Moreover, the cubic SrF<sub>2</sub> and CaF<sub>2</sub> crystals would effectively reduce the birefringence. However, high transparency means low optical scattering in FGCs, which is inconsistent with the scattering theory. Because the grain sizes of FGCs have reached the micron level. In this situation, the phase of the scattered light should be considered to lead to interference effects. In other words, it needs take spatial refractive index fluctuations into consideration, which takes into account all of the intricate and subtle spatial geometric features of the crystalline phase structure.<sup>49</sup> As for the slight decreases of transmittance in FGCMgF<sub>2</sub> to 60% in the range of 2–9  $\mu\text{m}$ , it can be explained by the low refractive index consistency and birefringence in tetragonal MgF<sub>2</sub> crystals. As the FGCs maintain the high infrared transmittance properties, as shown in Fig. 5b, FGCs demonstrate the similar image sharpness of fluorindate glass in infrared thermal imaging. This indicates that FGCs are favourable competitive materials for infrared detection, infrared imaging, infrared window, *etc.*

Further manifestations of FGCs as promising photonic materials are observed in the fluorescence properties studied in rare earth (RE) cations doping FGCs, taking advantage of their ultrawide transmittance, low phonon energy and high RE ions solubility. Notably, RE ions are proved to accumulate preferentially in crystalline phase in glass-ceramic materials, which will provide a low phonon energy environment conducive to luminescence.<sup>50,51</sup> Photon up-conversion (UC) is an *anti*-Stokes emission in which the sequential absorption of two or more photons leads to the emission of photons of shorter

wavelength than the excitation. The typical case is the conversion of infrared light to visible light. The fluoride materials are transparent from visible and IR regions with low phonon energy, which would decrease the non-radiative losses of RE cations to benefit their UC process.<sup>52</sup> As presented in Fig. 6a, the fluorescence emission spectra of FGCs by 2 mol% Er<sup>3+</sup> excited by a 980 nm laser diode shows two emission peaks in the visible region around 550 nm and 660 nm, respectively. These two intensive UC emissions are assigned to the Er<sup>3+</sup> energy transition of <sup>4</sup>S<sub>3/2</sub> → <sup>4</sup>I<sub>15/2</sub> (550 nm) and <sup>4</sup>F<sub>9/2</sub> → <sup>4</sup>I<sub>15/2</sub> (660 nm). Obviously, the UC fluorescence intensity of Er<sup>3+</sup> cations is enhanced in all FGCs than that in fluorindate glass, which can be attributed to the lower phonon energy of alkaline-earth fluoride crystals (MgF<sub>2</sub>(399 cm<sup>-1</sup>), CaF<sub>2</sub>(325 cm<sup>-1</sup>), SrF<sub>2</sub>(211 cm<sup>-1</sup>)) than that of fluorindate glass (~511 cm<sup>-1</sup>).<sup>22,31,53</sup> Additional proof for the suppression of multi-phonon nonradiative transition in Er<sup>3+</sup> doped FGCs has been observed in the fluorescence lifetime of the Er<sup>3+</sup>:<sup>4</sup>S<sub>3/2</sub> energy level (Fig. 6b), all the lifetimes of Er<sup>3+</sup> cations in FGCs (3.27 ms in FGCSrF<sub>2</sub>, 2.85 ms in FGCCaF<sub>2</sub> and 2.22 ms in FGCMgF<sub>2</sub>) is longer than that in fluorindate glass (1.96 ms). The calculation process are shown in Fig. S8 and Table S4 (ESI<sup>†</sup>).

Beyond UC emission, we demonstrated that the FGCs bears a promising MIR fluorescence performance by doping of 2 mol% Dy<sup>3+</sup>, as a result of their unique feature of intrinsic low phonon energy and broad MIR transmittance. The intense emission around 2.9  $\mu\text{m}$  by pumping at 1300 nm, corresponding to the Dy<sup>3+</sup>:<sup>6</sup>H<sub>13/2</sub> → <sup>6</sup>H<sub>15/2</sub> transition, were observed (Fig. 6c). It can be clearly seen the same evolution trend in 2.9  $\mu\text{m}$  fluorescence intensity of Dy<sup>3+</sup> as in the UC fluorescence of Er<sup>3+</sup>, which further manifests that the lower phonon energy of alkaline-earth fluoride crystals in FGCs result in the superior MIR fluorescence properties of Dy<sup>3+</sup>. The broadband emission of Dy<sup>3+</sup> covers the region of 2.6 to 3.4  $\mu\text{m}$  were maintained in FGCs. Such broadband emission shows great advantages in the fields of fiber amplifiers and tunable lasers in MIR.<sup>54</sup> The emission cross section ( $\sigma_{\text{em}}$ ) of the aforementioned transition is calculated from the absorption cross section by the reciprocity method of the McCumber theory,<sup>55</sup> as presented in Fig. 6d. The 2.9  $\mu\text{m}$  emission cross section of FGCMgF<sub>2</sub>, FGCCaF<sub>2</sub>, FGCSrF<sub>2</sub>



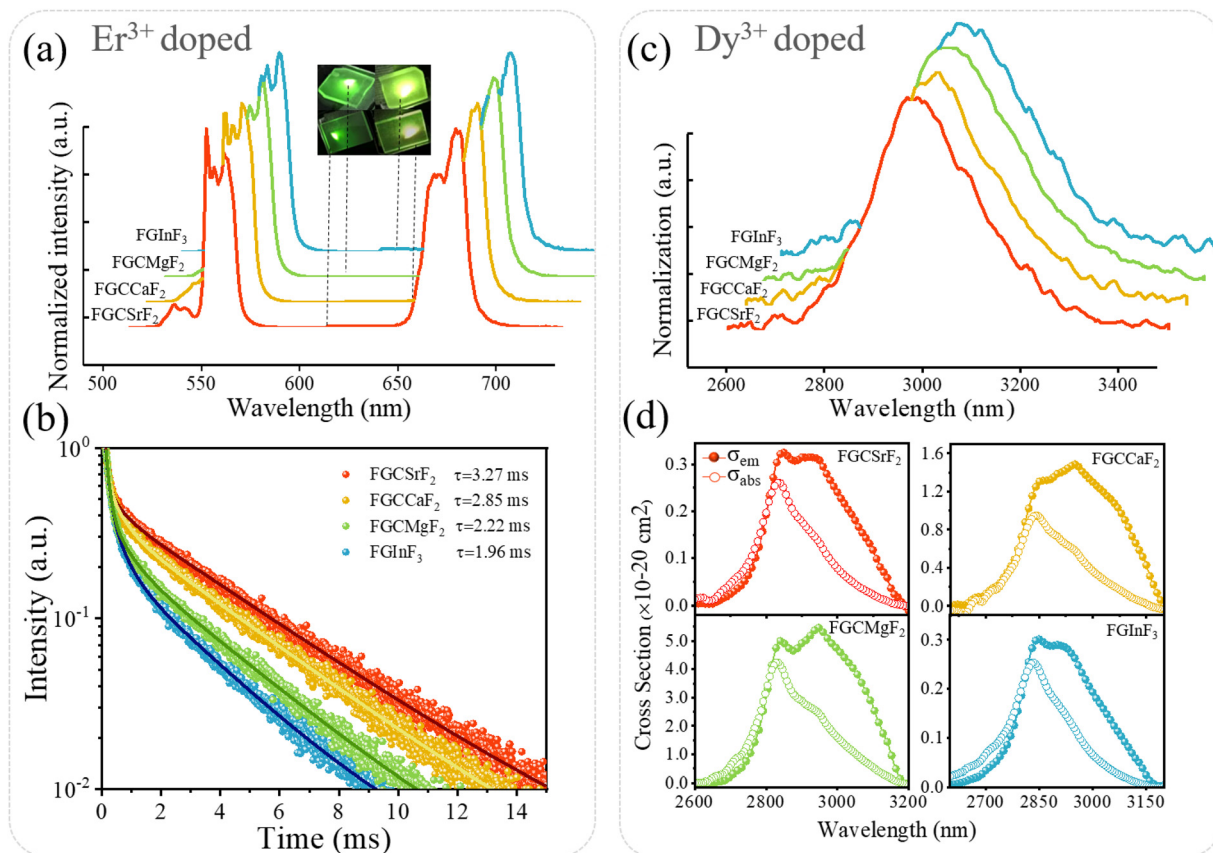


Fig. 6 UC and MIR fluorescence properties of RE doped FGCs. (a) UC emission spectra of Er<sup>3+</sup> doped FGCs and FGIInF<sub>3</sub> pumped at 980 nm; the illustration are UC luminescence pictures; (b) the decay curves of Er<sup>3+</sup>: <sup>4</sup>S<sub>3/2</sub> of the FGCs and FGIInF<sub>3</sub>. (c) MIR emission spectra around 2.9 μm of Dy<sup>3+</sup> doped FGCs and FGIInF<sub>3</sub> pumped at 1300 nm. (d) The emission cross sections around 2.9 μm obtained by absorption cross sections of Dy<sup>3+</sup> doped FGCs and FGIInF<sub>3</sub>.

and FGIInF<sub>3</sub> are  $5.5 \times 10^{-20} \text{ cm}^{-2}$ ,  $1.5 \times 10^{-20} \text{ cm}^{-2}$ ,  $0.33 \times 10^{-20} \text{ cm}^{-2}$  and  $0.3 \times 10^{-20} \text{ cm}^{-2}$ , separately. As the Dy<sup>3+</sup>: <sup>6</sup>H<sub>13/2</sub> → <sup>6</sup>H<sub>15/2</sub> transition is sensitive to the chemical environment where Dy<sup>3+</sup> cations locate, the larger emission cross section can be correlated with the incorporation of Dy<sup>3+</sup> into both the crystalline phase and the amorphous phase in FGCs. This higher emission probability of Dy<sup>3+</sup> in FGCs indicates the presence of alkaline-earth fluoride crystals in the fluorindate glass is more favourable for the MIR fluorescence.

## 4. Conclusions

This study introduces a compelling facile one-step route to the realization of FGCs with phase-selective crystallization. Here, a set of alkaline-earth cations were selected for the phase separation inducing nucleation and spontaneous crystallization in the fluoride glass melt owing to their high strength field. Subsequently, rapid quenching was employed to tailor the spontaneous crystallization in the cooling process. The atomic scale phase separated alkaline earth cations–fluoride anions rich domains were revealed by the AIMD simulations. The fabricated novel FGCs containing SrF<sub>2</sub>, CaF<sub>2</sub> or MgF<sub>2</sub> crystals, exhibit enhanced mechanical strength and chemical stability, longer IR cut-off wave length compared to the parent fluorindate glass. The rational phase separation engineering and thermodynamics in the rapid quenching were

unveiled in detail based on the variation in crystal morphology, element distribution, and atomic glass melt structure, *via* SEM, EDS mapping and AIMD simulations, respectively.

With Er<sup>3+</sup> cation doping, the FGCs show a longer lifetime than fluorindate glass. With Dy<sup>3+</sup> cation doping, the FGCs exhibit broadband MIR emission around 2.9 μm, especially, the larger emission cross sections were determined compared to Dy<sup>3+</sup> doped fluorindate glass. These characteristics indicate the introduction of lower phonon energy crystals provide the rich possibilities for tailoring fluorescence properties of RE cations from the visible to the IR range.

In summary, we have demonstrated how rational phase separation engineering *via* the field strength theory offers the feasibility for the phase-selective crystallization in the fluoride glass melt, combined with the rapid quenching, leading to a general facile one-step strategy for the fabrication of FGCs. The understanding of the complex fluoride glass melt chemistry and thermodynamics in the concurrent rapid-quenching and crystallization process, manifest a bright future for constructing the family of FGCs.

## Conflicts of interest

There are no conflicts to declare.



## Acknowledgements

This study was supported by the National Natural Science Foundation of China (No. 52002384 and 52002385), the Natural Science Foundation of Shanghai (19YF1453300), and the National Key Research and Development Program of China (No. 2021YFB3500901). J. H. acknowledges the Shanghai Pujiang Talent Plan (2020PJD079). B. D. acknowledges the National Institute for Materials Science under the Support system for curiosity-driven research, JSPS KAKENHI (No. JP21K14656), the Grant for Basic Science Research Projects from The Sumitomo Foundation and The Kao Foundation for Arts and Sciences.

## Notes and references

- X. Fan, J. Wang, X. Qiao, M. Wang, J.-L. Adam and X. Zhang, *J. Phys. Chem. B*, 2006, **110**, 5950–5954.
- Z. Chen, W. Cui, S. Kang, H. Zhang, G. Dong, C. Jiang, S. Zhou and J. Qiu, *Adv. Opt. Mater.*, 2017, **5**, 1600554.
- E. D. Zanotto, *Am. Ceram. Soc. Bull.*, 2010, **89**, 19–27.
- F. Serbena, I. Mathias, C. Foerster and E. Zanotto, *Acta Mater.*, 2015, **86**, 216–228.
- D. Tran, G. Sigel and B. Bendow, *J. Light Technol.*, 1984, **2**, 566–586.
- M. Brekhovskikh, L. Moiseeva, S. K. Batygov, I. Zhidkova and V. Fedorov, *Inorg. Mater.*, 2015, **51**, 1348–1361.
- M. G. Drexhage, *Treatise on Materials Science & Technology*, Elsevier, 1985, vol. 26, pp. 151–243.
- M. Mortier, A. Monteville, G. Patriarche, G. Mazé and F. Auzel, *Opt. Mater.*, 2001, **16**, 255–267.
- A. J. Stevenson, H. Serier-Brault, P. Gredin and M. Mortier, *J. Fluorine Chem.*, 2011, **132**, 1165–1173.
- M. Ferrari, E. Duval, A. Boyrivent, A. Boukenter and J. Adam, *J. Non-Cryst. Solids*, 1988, **99**, 210–221.
- J. Rousset, M. Ferrari, E. Duval, A. Boukenter, C. Mai, S. Etienne and J. Adam, *J. Non-Cryst. Solids*, 1989, **111**, 238–244.
- G. Wu, S. Fan, Y. Zhang, G. Chai, Z. Ma, M. Peng, J. Qiu and G. Dong, *Opt. Lett.*, 2013, **38**, 3071–3074.
- X. Xu, W. Zhang, D. Yang, W. Lu, J. Qiu and S. F. Yu, *Adv. Mater.*, 2016, **28**, 8045–8050.
- G. C. Jones and S. Houde-Walter, *J. Opt. Soc. Am. B*, 2005, **22**, 825–830.
- X. Liu, E. Mei, Z. Liu, J. Du, X. Liang and W. Xiang, *ACS Photonics*, 2021, **8**, 887–893.
- J. M. Jewell, E. J. Friebele and I. D. Aggarwal, *J. Non-Cryst. Solids*, 1995, **188**, 285–288.
- J. M. Jewell, E. J. Friebele and I. D. Aggarwal, *J. Am. Ceram. Soc.*, 1996, **79**(9), 2397–2402.
- C. Yu, J. Zhang and Z. Jiang, *J. Non. Cryst. Solids*, 2007, **353**, 2654–2658.
- F. Auzel, K. E. Lipinska-Kalita and P. Santa-Cruz, *Opt. Mater.*, 1996, **5**, 75–78.
- X. Hu, D. R. MacFarlane, P. Newman and A. Edgar, *J. Non-Cryst. Solids*, 2003, **326**, 177–183.
- M. O. Prado and E. D. Zanotto, *C. R. Chim*, 2002, **5**, 773–786.
- L. Zhang, Y. Jiang, Z. Wang, C. Yuan, M. Liao, J. Li and L. Zhang, *Opt. Lett.*, 2019, **44**, 4857–4860.
- Y. Jiang, L. Zhang, C. Yuan, Z. Wang, L. Wang, Y. Li, M. Liao and L. Zhang, *J. Eur. Ceram. Soc.*, 2020, **40**, 3244–3248.
- X. Huang, Y. Jiang, L. Zhang, F. Guan, Z. Wang, X. Yuan, J. He and L. Zhang, *J. Am. Ceram. Soc.*, 2022, **105**, 3959–3966.
- S. Liu, Y. Zhang and Y. Yue, *Phys. Chem. Glasses: Eur. J. Glass Sci. Technol., Part B*, 2011, **52**, 231–235.
- S. Liu, Y. Zhang and Y. Yue, *Phys. Chem. Glasses: Eur. J. Glass Sci. Technol., Part B*, 2011, **52**, 85–90.
- O. V. Mazurin and E. Porai-Koshits, *Phase separation in glass*, Elsevier, 1984.
- P. James, *J. Mater. Sci.*, 1975, **10**, 1802–1825.
- L. Zhang, F. Guan, L. Zhang and Y. Jiang, *Opt. Mater. Express*, 2022, **12**, 1683–1707.
- H. G. Lipson, B. Bendow, N. E. Massa and S. S. Mitra, *Phys. Rev. B: Solid State*, 1976, **13**, 2614.
- W. Ma, X. Qian, J. Wang, J. Liu, X. Fan, J. Liu, L. Su and J. Xu, *Sci. Rep.*, 2016, **6**, 1–7.
- J. F. G. Kresse, *Phys. Rev. B: Condens. Matter Mater. Phys.*, 1996, **54**, 11169–11186.
- X. Liu, G. Chen, H. Hou, X. Hui, K. Yao, Z. Lu and C. Liu, *Acta Mater.*, 2008, **56**, 2760–2769.
- T. S. Ingebrigtsen, J. C. Dyre, T. B. Schrøder and C. P. Royall, *Phys. Rev. X*, 2019, **9**, 031016.
- F. Meng, Y. Sun, F. Zhang, B. Da, C.-Z. Wang, M. J. Kramer, K.-M. Ho and D. Sun, *Phys. Rev. Mater.*, 2021, **5**, 043402.
- J. Málek, *Thermochim. Acta*, 1995, **267**, 61–73.
- A. Astaf'ev and L. Levitan, *Met. Sci. Heat Treat.*, 1999, **41**, 54–57.
- A. Horn and M. Merklein, 2021.
- CRC handbook of chemistry and physics, CRC Press, 2004.
- H. Keith and F. Padden Jr, *J. Appl. Phys.*, 1963, **34**, 2409–2421.
- F. Frank, in *Proceedings*, ed., R. H. Doremus, B. W. Roberts and D. Turnbull, Wiley, New York, 1958.
- J. Fan, S. Chen, X. Yuan, Y. Jiang, L. Pan, B. Jiang, X. Mao, R. Li, X. Jiang and L. Zhang, *J. Am. Ceram. Soc.*, 2016, **99**, 2971–2976.
- R.-G. Duan, K.-M. Liang and S.-R. Gu, *Mater. Res. Bull.*, 1998, **33**, 1143–1149.
- R. Almeida, J. Pereira, Y. Messaddeq and M. A. Aegerter, *J. Non-Cryst. Solids*, 1993, **161**, 105–108.
- S. Bakhvalov, E. Petrova, A. Livshits, A. Shubin, V. Buznik and V. Denisov, *J. Struct. Chem.*, 1998, **39**, 651–659.
- Y. Akasaka, T. Nanba, H. Inoue, T. Osuka and I. Yasui, *J. Non-Cryst. Solids*, 1992, **140**, 249–254.
- K. Shinozaki, W. Pisarski, M. Affatigato, T. Honma and T. Komatsu, *Opt. Mater.*, 2015, **50**, 238–243.
- X. Fang, C.-Z. Wang, S. Hao, M. J. Kramer, Y. Yao, M. Mendelev, Z. Ding, R. Napolitano and K.-M. Ho, *Sci. Rep.*, 2011, **1**, 1–5.
- N. Borrelli, A. Mitchell and C. Smith, *J. Opt. Soc. Am. B*, 2018, **35**, 1725–1732.
- Z. Gao, X. Lu, Y. Chu, S. Guo, L. Liu, Y. Liu, S. Sun, J. Ren and J. Yang, *J. Mater. Chem. C*, 2018, **6**, 2944–2950.

- 51 Z. Gao, S. Guo, X. Lu, J. Orava, T. Wagner, L. Zheng, Y. Liu, S. Sun, F. He and P. Yang, *Adv. Opt. Mater.*, 2018, **6**, 1701407.
- 52 S. Han, R. Deng, X. Xie and X. Liu, *Angew. Chem., Int. Ed.*, 2014, **53**, 11702–11715.
- 53 D. Jiang, Y. Zhan, Q. Zhang, F. Ma, L. Su, F. Tang, X. Qian and J. Xu, *CrystEngComm*, 2015, **17**, 7398–7405.
- 54 J. Ren, X. Lu, C. Lin and R. Jain, *Opt. Express*, 2020, **28**, 21522–21548.
- 55 D. McCumber, *Phys. Rev.*, 1964, **136**, A954.